nanomaterials

MDPI

Article

A Single-Celled Metasurface for Multipolarization Generation and Wavefront Manipulation

Ruonan Ji [1,*], Xin Guo [2], Zhichao Liu [3], Xianfeng Wu [1], Chuan Jin [3], Feng Liu [1], Xinru Zheng [1], Yang Sun [1] and Shaowei Wang [4,*]

[1] School of Physical Science and Technology, Northwestern Polytechnical University, Xi'an 710129, China
[2] Science and Technology on Low-Light-Level Night Version Laboratory, Xi'an 710065, China
[3] State Key Laboratory of Transient Optics and Photonics, Xi'an Institute of Optics and Precision Mechanics of CAS, Xi'an 710119, China
[4] State Key Laboratory for Infrared Physics, Shanghai Institute of Technical Physics, Chinese Academy of Sciences, Shanghai 200083, China
* Correspondence: jiruonan@nwpu.edu.cn (R.J.); wangshw@mail.sitp.ac.cn (S.W.)

Abstract: Due to their unprecedented ability to flexibly manipulate the parameters of light, metasurfaces offer a new approach to integrating multiple functions in a single optical element. In this paper, based on a single-celled metasurface composed of chiral umbrella-shaped metal–insulator–metal (MIM) unit cells, a strategy for simultaneous multiple polarization generation and wavefront shaping is proposed. The unit cells can function as broadband and high-performance polarization-preserving mirrors. In addition, by introducing a chiral-assisted Aharonov–Anandan (AA) geometric phase, the phase profile and phase retardation of two spin-flipped orthogonal circular polarized components can be realized simultaneously and independently with a single-celled metasurface via two irrelevant parameters. Benefiting from this flexible phase manipulation ability, a vectorial hologram generator and metalens array with spatially varying polarizations were demonstrated. This work provides an effective approach to avoid the pixel and efficiency losses caused by the intrinsic symmetry of the PB geometric phase, and it may play an important role in the miniaturization and integration of multipolarization-involved displays, real-time imaging, and spectroscopy systems.

Keywords: metasurface; polarization generation; wavefront shaping; Aharonov–Anandan (AA) geometric phase

Citation: Ji, R.; Guo, X.; Liu, Z.; Wu, X.; Jin, C.; Liu, F.; Zheng, X.; Sun, Y.; Wang, S. A Single-Celled Metasurface for Multipolarization Generation and Wavefront Manipulation. *Nanomaterials* **2022**, *12*, 4336. https://doi.org/10.3390/nano12234336

Academic Editors: Onofrio M. Maragò and Bouchta Sahraoui

Received: 10 November 2022
Accepted: 2 December 2022
Published: 6 December 2022

1. Introduction

Polarization is an inherent property of light which is essential for many applications, such as polarization detection and imaging, nonlinear optics, three-dimensional displays, and data storage and transfer. In many polarization-involved applications, such as polarization detection or imaging for dynamic or living targets, multipolarization displays, and polarization multiplexing, multipolarization generation and manipulation are required. Linear polarizers and waveplates are traditional optical elements for polarization generation and manipulation. However, with a single polarizer, only one polarization can be filtered, and the generation of circular polarization requires cascading linear polarizers and quarter waveplates. Therefore, in general, lots of optical elements for polarization generation and wavefront manipulation are needed for a multipolarization-involved system, which makes them bulky and complicated. How to obtain miniaturized optical elements with functions of multipolarization generation and manipulation is significant for the development of multipolarization-involved systems.

The emergence of metasurfaces has provided a promising and artful approach to solving the above problem. Benefiting from an unprecedented and flexible capability in the manipulation of the intensity, polarization, and phase of light [1–3], recent years have witnessed the development of various metasurface-based devices, such as metalenses [4–7],

vortex generators [8–13], holograms [2,9,14–17], metagratings [1,18], nanoprints [19–22], and so on. Among them, in terms of polarization conversion, imposing different phase retardations on orthogonal linear/circular polarizations is the general design strategy [10,23,24]. The propagation phase and geometric phase are two basic phase types used in the design of a metasurface [25]. Therein, the geometric phase is introduced during the SU(2) manipulation with the polarization state on the Poincare sphere, namely, in the process of the circular polarization conversion (spin flipping). Moreover, different from the propagation phase, the geometric phase is independent of the frequency and only related to the geometric path of evolution, i.e., the angle of rotation of the polarization ellipse from the perspective of Coriolis shift. Thus, the geometric phase is favored by researchers due to its advantage of nondispersive modulation on phase, and the Pancharatnam–Berry (PB) geometric phase is the first proposed and most widely used geometric phase [23,26,27]. When contrarotating the anisotropic structure by angle θ, the angle of rotation of the polarization ellipses corresponding to the right-handed circular polarized (RCP) and left-handed circular polarized (LCP) phases are the same values but in opposite directions. Then a PB phase shift of $\pm 2\theta$ will be introduced to the spin-flipped component, and herein, the RCP light takes a negative sign while the LCP light takes a positive sign. Such intrinsic symmetry makes it impossible to achieve arbitrary control of the polarization state with a single-celled scheme. Once the phase distribution of LCP light is set, the one for RCP light is fixed. For example, if the metasurface phase profile under LCP incidence is set for focusing, the metasurface will diverge the RCP incidence. As a compromised solution, arranging two or more nanostructures respectively manipulating the LCP and RCP localized phases as a supercell to form an interleaved metasurface is widely employed [23,24]. However, such a configuration may bring an unavoidable loss of pixels and low energy efficiency.

Very recently, another geometric phase, the nonadiabatic Aharonov–Anandan (AA) phase was introduced in the design of a metasurface [9,10,28]. In the scheme of the nonadiabatic AA phase, the structure parameters are changed to rotate the polarization ellipse and therefore introduce geometric phase shift. In this way, it provides a promising approach to decouple the angle of rotation of the polarization ellipses respectively corresponding to the RCP and LCP phases. Therefore, as a kind of geometric phase, the AA phase has attracted much attention as it not only possesses the advantage of nondispersive phase control but also has the potential to artfully avoid the intrinsic symmetry of LCP and RCP phases [9,28,29]. Benefiting from such merit and the spin-dependent response of the chiral structure, an umbrella-shaped metasurface was proposed as an example to verify the validity of the spin-decoupled AA phase manipulation mechanism. Then, a combined geometric phase metasurface for dual manipulations was proposed to realize simultaneous holography/vortex generation and polarization rotation [10]. While in previous work, the AA phase was introduced to break the intrinsic symmetry of the PB geometric phase. As the change of the PB phase led to a chain response of both phases of LCP and RCP, the desired AA phase profile needed to be obtained by some calculation. In this work, analogous to the optical activity process in traditional media, a spin-decoupled AA phase manipulation mechanism was further applied to achieve broadband and achromatic optical activity, and a new design scheme of single-celled metasurfaces which perform bifunctional polarization control and wavefront shaping was proposed. The design of the metasurface was further simplified, as only the AA geometric phase was applied, and the phase profile of the LCP and RCP components were independently controlled by two irrelevant parameters. Based on the proposed strategy, a vectorial hologram generator and metalens for multiple polarization generation and focusing were proposed, which may have a far-reaching influence on the miniaturization of multipolarization-involved optical systems.

2. Working Principle and Unit Cell Design

According to the theory of optical activity proposed by Fresnel, when a linear polarized (LP) light incident is in a media with optical activity, the LP state can be decomposed into two orthogonal circular polarization states with equal amplitude. The polarization rotation angle

of the transmitted light is determined by the phase retardation δ between the LCP and RCP components. Such a relationship can be expressed as Equation (1) with a Jones vector [10]:

$$|LP\rangle = \begin{bmatrix} cos\varphi \\ sin\varphi \end{bmatrix} = \frac{\sqrt{2}}{2} e^{-i\varphi} \left(e^{i2\varphi} \left| LCP \right\rangle + |RCP\rangle \right) = \frac{\sqrt{2}}{2} e^{-i\varphi} \left(e^{i\delta} \left| LCP \right\rangle + |RCP\rangle \right) \quad (1)$$

where $\varphi = \delta/2$ is the polarization rotation angle, and $|LP\rangle$, $|LCP\rangle$, and $|RCP\rangle$ are the polarization states of LP, LCP, and RCP light, respectively.

Analogous to the optical activity process in traditional media, in this paper, a metasurface with meta-atoms capable of manipulating the phases of RCP and LCP components independently was introduced. Since the geometric phase is generated during the spin-flipping of circularly polarized light, the meta-atom was designed as a three-layered MIM structure (see Figure 1a) with broadband and high circular polarization preserving ability (in the reflection scheme, spin-flipping components correspond to circular polarization preserving components, i.e., R_{LL} and R_{RR}; here, the first and second subscripts represent the handedness of the reflected and incident light, respectively) [9]. The optical properties of the meta-atoms were simulated based on the finite element method (FEM). Detailed information about the simulation method is described in the Appendix A, and a discussion on the efficiency of the designed meta-atom (see Figure S1) can be found in Supplementary Materials. The umbrella-shaped nanostructure on the top introduced a spin-dependent response due to the chiral configuration, and our previous study showed LCP and RCP incident light mainly interact with the left and right parts of the nanostructure, respectively. Moreover, different from normal anisotropic structures like nanobrick, the principal axis of the umbrella-shaped structure was determined by the lengths of the left and right arms. These features provided an effective approach to generate spin-independent rotation of the polarization ellipse without rotating the structure. As shown in Figure 1b,c, when the value of β is fixed, the increase of α will bring an evolution of φ_{LL} (the phase of R_{LL}) varying from 0° to 360° while φ_{RR} (the phase of R_{RR}) remains nearly constant at the same wavelength. A similar phenomenon can be observed when α is fixed and β changes, except that φ_{LL} and φ_{RR} are interchanged. Moreover, for structures with the same α and β, the phase retardation δ is stable in the whole operation band. In the other words, when an x-LP (i.e., LP polarization with polarization direction along the x-axis) incident interacts with the meta-atom, an achromatic phase retardation δ will introduce the two spin-flipped reflection components. Meanwhile, the intensity difference between the two components (R_{LL} and R_{RR}) is small enough to be ignored. Thus, these two components are coupled in the near-field and contribute to broadband and achromatic optical activity effects. By synchronously controlling φ_{LL}, φ_{RR}, and δ, it is possible to independently control the wavefront as well as the polarization state of reflection in a single-celled metasurface.

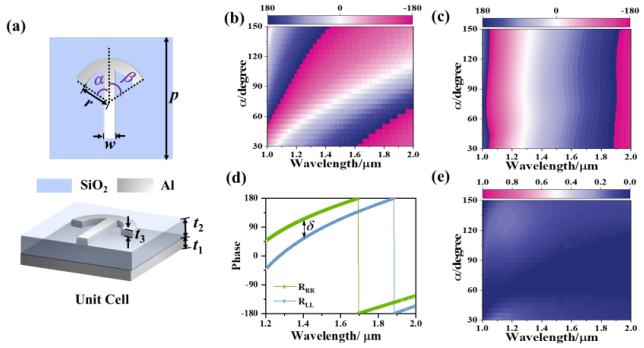

Figure 1. (**a**) Schematic diagram of the unit cell (**b**,**c**) phase of spin-flipped reflection. (**b**) φ_{LL} and (**c**) φ_{RR} varies with central angle α (**d**) phase retardation between φ_{LL} and φ_{RR} in the range of 1–2 μm when α = 40° and β = 60°. (**e**) Reflection difference between spin-flipped reflection R_{LL} and R_{RR} varies with central angle α. In these simulations, p = 700 nm, r = 120 nm, w = 80 nm, t_1 = 200 nm, t_2 = 180 nm, t_3 = 100 nm. Specifically, in (**b**,**c**,**e**), α varies from 30° to 150° and β = 60°.

3. Metasurface for Vectorial Holography

Vectorial metaholography refers to a hologram diffracts holographic images with spatially varying polarization states, as shown in Figure 2a. Compared to conventional scalar holography, vectorial holography records intensity, phase, and polarization features, which largely increases the information capacity carried by the light wavefront [30]. In previous reports, due to the intrinsic spin symmetry of the PB geometric phase, a meta-molecule composed of at least two orthogonal meta-atoms was needed to control the phase retardation, leading to the unavoidable loss of pixels [31]. Benefiting from the flexible phase control of the proposed single-celled metasurface, a vectorial metahologram containing 0°, 45°, 90°, and RCP polarization states was presented experimentally.

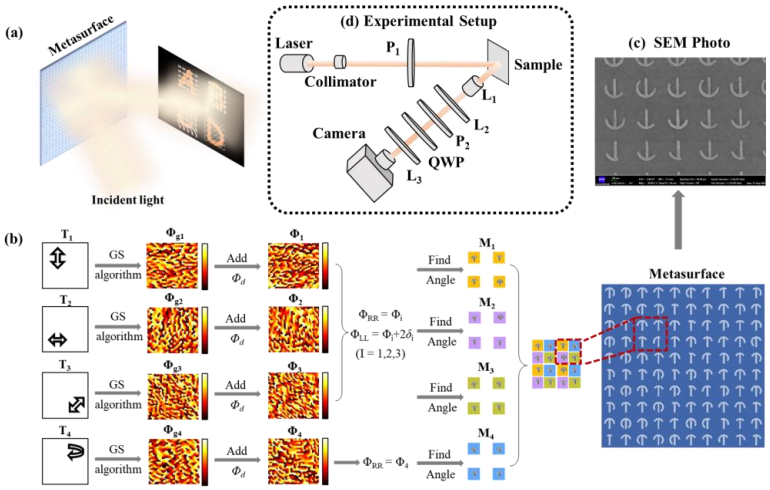

Figure 2. (**a**) Schematic diagram of vectorial holography with spatially varying polarization. (**b**) The design process of the metasurface for vectorial metaholography. (**c**) SEM photo of the fabricated sample. (**d**) Experimental setup for vectorial hologram polarization-sorting process (P_1–polarizer 1, P_2–polarizer 2, L_1–objective lens, L_2–lens 2, L_3–lens 3, QWP–quarter waveplate. In the test, QWP is only used for the sorting of circular polarization).

The design process of the metasurface is shown in Figure 2b. Based on the Gerchberg–Saxton (GS) algorithm for the phase-only hologram, the phase profiles Φ_{g1}, Φ_{g2}, Φ_{g3}, and Φ_{g4} of the four target images were calculated. Phase gradient Φ_d along the x-axis providing a 20° deflection was introduced to avoid the influence of the spin-preserving components. Then, the four-phase distributions were respectively encoded onto the single-celled metasurfaces M_1, M_2, M_3, and M_4, and interleaved to form the final sample. Herein, in the design of M_1, M_2, and M_3, the value of φ_{RR} at each pixel was modulated by changing the central angle β of each unit cell, and $\varphi_{RR} = \Phi_{gi} + \Phi_d$ (i = 1,2,3). In addition, the value of φ_{LL} was modulated by changing the central angle α, and $\varphi_{LL} = \Phi_{gi} + \Phi_d + 2\delta$ (i = 1, 2, 3), where δ is the polarization rotation angle regarding the polarization direction of the incident light; the values are 90, 0, and 45, respectively. As for M_4, central angle α was fixed at 60° while $\varphi_{RR} = \Phi_{g4} + \Phi_d$ was encoded in each central angle β of the metasurface.

The designed metasurface was fabricated via a typical lift-off process. Figure 2c,d shows the SEM photo of the fabricated sample with 400 × 400 meta-atoms and the experimental setup of the vectorial holography testing. A fiber laser operating at 1.55 μm was used as the light source; after being collimated, the light passed through a polarizer to generate a normally incident LP light. The target images were reconstructed via the Fourier transform of the objective lens, and the polarization states of the images were examined by polarizer or the combination of a polarizer and quarter waveplate. More detailed fabrication and testing information can be found in the Appendix A. Due to the limited computer memory, the four metasurfaces (M_1–M_4) for different target reconstructions were simulated separately, and the dimension of the arrays was chosen as 50 × 50. As shown in Figure 3a,

the simulated results verify the broadband working ability, as similar reconstructed images of the targets can be observed from 1.2 μm to 2 μm. In the process of diffraction, the size of the reconstructed image is proportional to the wavelength; thus, it can be found that the reconstructed image size gradually increases from 1.2 to 2 μm. Then, the feature of spatially varying polarizations was verified by an experimental polarization-sorting test. Upon rotation of polarizer P_2, the reconstructed image of circularly polarized targets T_4 was almost unchanged while the linearly polarized targets (T_1, T_2, and T_3) showed obvious polarization characteristics. Specifically, as shown in Figure 3b, when the angle between polarizer P_1 and P_2 changed from 45° to −45°, the reconstructed image of T_3 changed from clear to nearly disappeared. After adding a quarter waveplate before P_2 and rotating P_2, it can be observed that the reconstructed image of T_1-T_3 was almost unchanged while the reconstructed image of T_4 sequentially changed from dimmed to clearly as the polarization state of the analyzer changed from RCP to LCP. Here, the phenomenon that the reconstructed image cannot completely disappear may mainly be caused by the fabrication error. The errors in structure parameters not only influence the phase but also bring a bigger difference between the R_{LL} and R_{RR} of each atom, which finally changes the combined reflection from quasilinear to elliptical polarized, and such a problem can be improved by optimizing the fabrication processes.

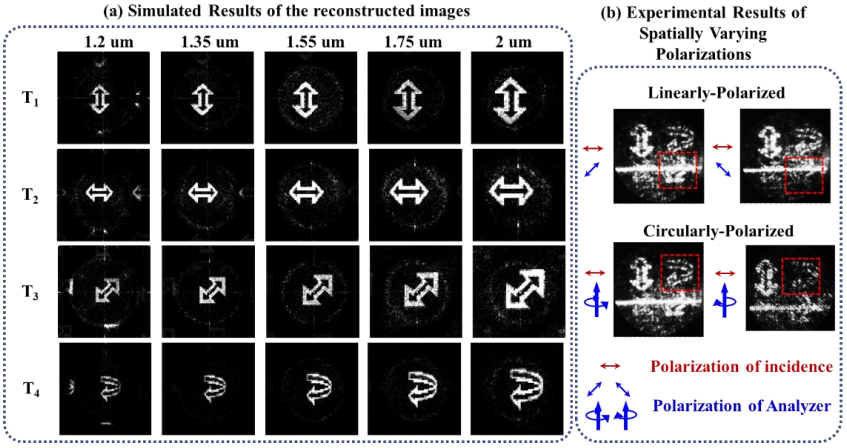

Figure 3. (**a**) Simulated results of reconstructed images at different wavelengths. (**b**) Experimental results of sorting spatially varying polarizations (λ = 1.55 μm).

4. Metasurface for Spatially Varying Foci and Polarization States

Traditional lenses are based on the refraction scheme of geometric optics, the phase accumulation during the propagation of light. Thus, they are generally bulky and nonplanar, as the thickness of the lens is determined by the required phase distribution, which is usually curved. On the contrary, the phase profile of a metalens is controlled by the optical response of each meta-atom and, therefore, metalenses can obtain a curved phase profile with a planar and ultrathin configuration [4–6,32,33]. As fundamental optical elements, metalenses have shown promising applications in miniaturized and integrated optical systems for optical imaging, spectroscopic analysis and measurement, lithography, and so on.

In this paper, benefiting from the exotic properties of the proposed single-celled metasurfaces, a metalens array simultaneously providing focusing and multiple polarization state generation is proposed. As shown in Figure 4a, when an LP light incident on the metasurface, the reflection light will split into multiple beams, and the polarization state and focal point of each beam can be designed independently and arbitrarily. This feature can be used to generate light sources with multiple polarization states in the polarization measuring system. Based on such kinds of optical sources, results corresponding to multiple polarization states can be synchronously obtained through a single measurement, which can greatly improve the efficiency of testing. Moreover, it provides a solution

for the problem of dynamic or living target measurement in the traditional time-sharing polarization system.

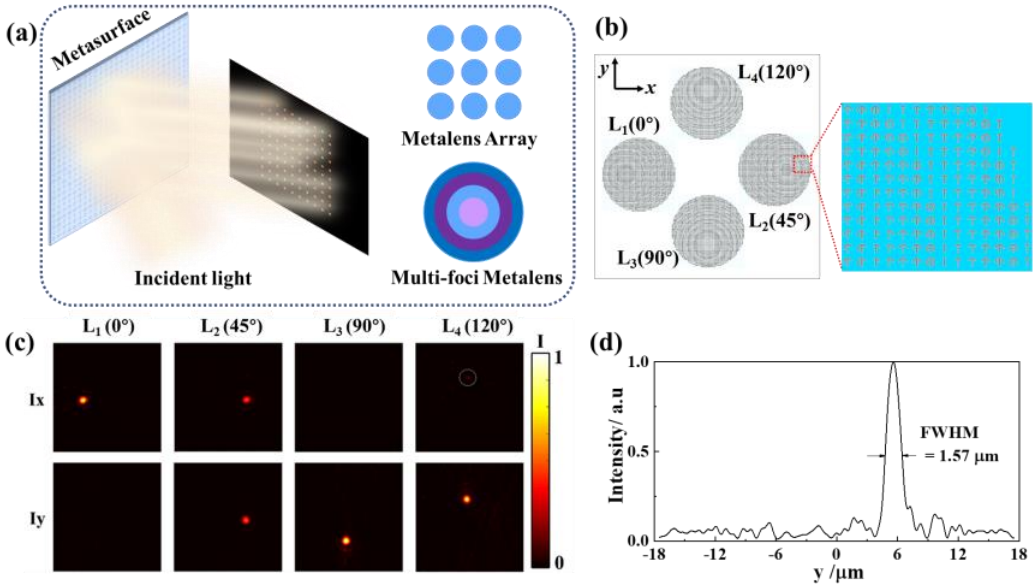

Figure 4. (**a**) Schematic diagram of metasurface with spatially varying focal spots and polarization states. The right two inserts show the two design schemes for obtaining spatially varying focal spots. (**b**) Schematic diagram of the designed metalens array. (**c**) Simulated x and y components of the focal spot intensity on the x–y plane (z = 33 μm); the generated polarization states are designed as 0°, 45°, 90°, and 120° for L_1, L_2, L_3, and L_4, respectively. (**d**) The intensity distribution of focal spot (L_2, 1.55 μm) along the y-axis (x = 0 μm, z = 33 μm).

The desired phase profile for an ideal lens can be written as Equation (2) [4]:

$$\Phi(x,y) = \frac{2\pi}{\lambda}\left(\sqrt{(x^2+y^2+f^2)} - f\right) \quad (2)$$

where λ is the operation wavelength, and f is the focal length. Metalens arrays and multifoci lenses are two common schemes to achieve multiple focal spots [4]. In this paper, the metalens array scheme was chosen and a four-metalens array with polarization rotation of 0°, 45°, 90°, and 120° was demonstrated to prove the validity of the strategy as shown in Figure 4b. Each metalens was composed of 50 × 50 single-celled meta-atoms. The operation wavelength and focal length were set as 1.55 μm and 35 μm, respectively. To combine the polarization rotation and focusing ability in the metalens, the corresponding phase profile can be expressed as Equations (3) and (4).

$$\Phi_{RR}(x,y) = \frac{2\pi}{\lambda}\left(\sqrt{(x^2+y^2+f^2)} - f\right) \quad (3)$$

$$\Phi_{LL}(x,y) = \frac{2\pi}{\lambda}\left(\sqrt{(x^2+y^2+f^2)} - f\right) + 2\delta \quad (4)$$

where the values of δ were set as 0°, 45°, 90°, and 120° for the four lenses, respectively. In addition, to fully split the four beams as well as avoid the influence of the spin-preserving components, the focused beams of the four lenses were set off-axis with deflection angles of 10° by adding a corresponding phase gradient, as shown in Figure 3b.

The electric field distributions under the x-LP light of each metalens were simulated, and the far-field diffraction spots were calculated based on the vector diffraction theory. As shown in Figure 4c, the simulated focal spots showed obvious polarization features. By extracting the spot intensities in the x and y polarization directions, the polarization states

of the four emergent lights could be calculated according to the *x*-pol and *y*-pol components of the spot. The results were quite close to 0°, 45°, 90°, and 120°, which also well match the design values. Figure 4d shows the intensity distribution of the focal spot along the *y*-axis with a 1.55 μm *x*-LP light incident on L_2. The full-width at half-maximum (FWHM) was 1.57 μm, indicating the designed metalenses have pretty good focusing performance.

The intensity distribution of the designed lenses at different wavelengths was also simulated to show the broadband operation property. As shown in Figure 5, the lenses showed favorable focusing characteristics at 1.55 μm and 2 μm. The focus length of the four designed lenses under the incidence of 1.55 μm were, respectively, 31.5 μm, 33.1 μm, 33.6 μm, and 36.2 μm, which are quite close to the designed focal length f = 35 μm. This difference in focal length was mainly caused by the limited size of the designed lens and the phase difference between the actual phase and the ideal phase. By further increasing the lens size and further optimizing the actual phase distribution, both the actual focal length accuracy and focusing performance can be improved. According to the relationship between the phase gradient and deflection angle, for the same phase gradient, the longer the wavelength, the larger the deflection angle. It should be noted here that the metalenses are chromatic. In this design, the phase gradients for focusing and deflection were designed with a center wavelength of 1.55 μm; thus, compared with the results corresponding to 1.55 μm, the focal lengths under the incidence of 2 μm were much shorter (about 23 μm), as shown in Figure 5. The metalenses can also be designed achromatically by using some optimization algorithms [5]. Moreover, Tsilipakos et al. recently proposed an ingenious approach for the phase compensation of different frequencies by utilizing trains of multiple resonances [34]; such a strategy may also inspire an achromatic design of the proposed metalenses.

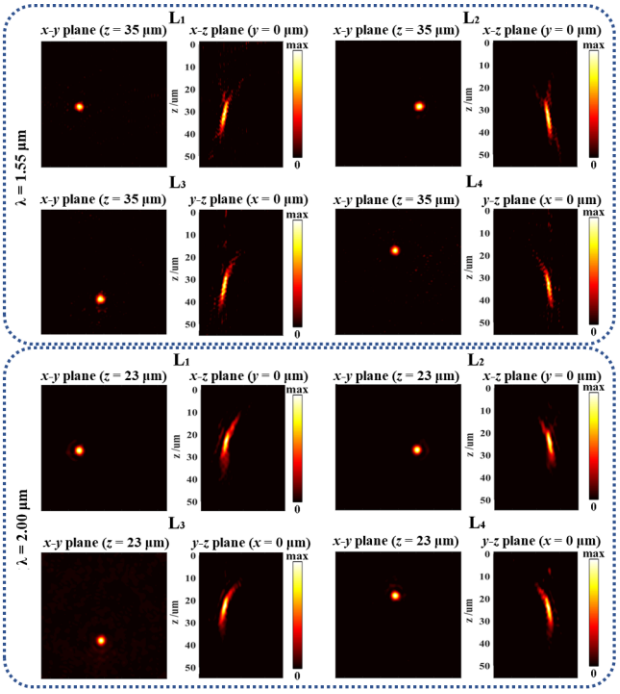

Figure 5. Intensity distributions of the designed lenses under incidence with different wavelengths.

5. Conclusions

In this paper, a single-celled metasurface composed of chiral umbrella-shaped MIM unit cells is proposed for multiple polarization generation and wavefront shaping. The unit cells were designed as broadband and high-performance polarization-preserving mirrors, which provide the basic condition for wavefront shaping based on the geometric phase. By introducing the manipulation of the AA geometric phase, the independent

manipulation of the phase and phase retardation of the spin-flipped components can be realized simultaneously and independently in a single unit cell. The above features finally contributed to independent control of the wavefront as well as the polarization state of reflection in a single-celled metasurface. To prove the validity of the proposed scheme, a vectorial hologram generator and metalens array with spatially varying polarizations were demonstrated, and both the simulated and experimental results agreed well with the design. Compared with the previous work based on the PB geometric phase, the proposed scheme in this paper can effectively avoid the pixel and efficiency losses caused by the intrinsic symmetry of the PB geometric phase. In addition, by virtue of the advantage of spin-independent control of the phase, no additional complicated algorithms were needed in the design. We believe this work will provide a new idea in the design of optical elements applied in miniaturized and integrated multipolarization-involved display, real-time imaging, or spectroscopy systems.

Supplementary Materials: The following supporting information can be downloaded at https://www.mdpi.com/article/10.3390/nano12234336/s1, Figure S1: Simulated spin-flipped component reflectance color maps of the unit cells. Ref. [35] is cited in the supplementary materials.

Author Contributions: The simulation was carried out by R.J. and X.W. The experiment was carried out by X.G., C.J. and F.L. The analyses and discussions of the obtained results were carried out by R.J., Y.S. and Z.L. The original draft was written by R.J. and X.Z. and S.W. reviewed and edited the original draft. All authors have read and agreed to the published version of the manuscript.

Funding: This research was funded by The National Natural Science Foundation of China, grant number 61805204, and The Natural Science Basic Research Plan in Shaanxi Province of China, grant number 2019JQ-133.

Institutional Review Board Statement: Not applicable.

Informed Consent Statement: Not applicable.

Data Availability Statement: Not applicable.

Acknowledgments: The authors would like to thank Liming Wang from Xidian University and Xi'an Leading Optoelectronic Technology Co., Ltd. for helping with the sample measurement.

Conflicts of Interest: The authors declare no conflict of interest.

Appendix A

Numerical Simulation Methods: The optical properties of the meta-atoms and performance of metasurfaces were simulated based on the finite element method (FEM). In the simulations of meta-atoms, periodic and waveguide port boundary conditions were applied to x(y) and z directions, respectively. In terms of the simulations of metasurfaces, open boundary conditions were applied, and a normally incident plane wave from positive direction of the z-axis was set as the light source. The optical constants of Al were taken from the report by Palik [36], and the index of refraction of SiO_2 was set as 1.5. The structure parameters were p = 700 nm, r = 120 nm, w = 80 nm, t_1 = 200 nm, t_2 = 180 nm, t_3 = 100 nm.

Fabrication Methods: The metasurface of vectorial metahologram generator was fabricated by a lift-off process. Firstly, 80 nm and 200 nm thick aluminum and silicon oxide films were sequentially deposited on a cleaned silicon substrate by electron beam evaporation (EBE, Kurt J. Lesker LAB line PVD 75) and plasma enhanced chemical vapor deposition (PECVD, Oxford PlasmaPro 100 PECVD) processes, respectively. Secondly, a 100 nm positive electron-beam resist (ZEP520A) was spin-coated on the silicon oxide film. In addition, a conductive protective coating was spin-coated on the resist to dissipate e-beam charges on insulating substrates during electron-beam lithography (EBL) process. Thirdly, a standard EBL (JEOL JBX-9500FS at 100 keV) process was applied to form a pattern mask. Finally, after depositing 50 nm aluminum film with the EBE process, the metasurface was obtained after removing the remaining resist in acetone.

Vectorial Metahologram Test: A self-built light path was used for the sample test. A 1550 nm fiber laser was used as the light source. Then, the light passed through a collimator and polarizer to generate normally incident LP incidence. After being reflected by the sample, the light was collected, and then the phase information was transformed into reconstructed image with an objective lens. Before being detected by an infrared camera, a 4f system with two lenses was used to adjust the size of the image. The operation range of the infrared camera (Leading 640 SWIR camera LD-SW6401725-CTE2-G) was from 900 to 1700 nm, and the active area and pixel size were 16 × 12.8 mm and 25 μm, respectively.

References

1. Yu, N.; Genevet, P.; Kats, M.A.; Aieta, F.; Tetienne, J.-P.; Capasso, F.; Gaburro, Z. Light Propagation with Phase Discontinuities: Generalized Laws of Reflection and Refraction. *Science* **2011**, *334*, 333–337. [CrossRef] [PubMed]
2. Guo, X.; Zhong, J.; Li, B.; Qi, S.; Li, Y.; Li, P.; Wen, D.; Liu, S.; Wei, B.; Zhao, J. Full-Color Holographic Display and Encryption with Full-Polarization Degree of Freedom. *Adv. Mater.* **2022**, *34*, 2103192. [CrossRef] [PubMed]
3. Du, K.; Barkaoui, H.; Zhang, X.; Jin, L.; Song, Q.; Xiao, S. Optical Metasurfaces towards Multifunctionality and Tunability. *Nanophotonics* **2022**, *11*, 1761–1781. [CrossRef]
4. Zang, X.; Ding, H.; Intaravanne, Y.; Chen, L.; Peng, Y.; Xie, J.; Ke, Q.; Balakin, A.V.; Shkurinov, A.P.; Chen, X.; et al. A Multi-Foci Metalens with Polarization-Rotated Focal Points. *Laser Photonics Rev.* **2019**, *13*, 1900182. [CrossRef]
5. Khorasaninejad, M.; Shi, Z.; Zhu, A.Y.; Chen, W.T.; Sanjeev, V.; Zaidi, A.; Capasso, F. Achromatic Metalens over 60 Nm Bandwidth in the Visible and Metalens with Reverse Chromatic Dispersion. *Nano Lett.* **2017**, *17*, 1819–1824. [CrossRef]
6. Wang, W.; Yang, Q.; He, S.; Shi, Y.; Liu, X.; Sun, J.; Guo, K.; Wang, L.; Guo, Z. Multiplexed Multi-Focal and Multi-Dimensional SHE (Spin Hall Effect) Metalens. *Opt. Express* **2021**, *29*, 43270. [CrossRef]
7. Ji, R.; Jin, C.; Song, K.; Wang, S.-W.; Zhao, X. Design of Multifunctional Janus Metasurface Based on Subwavelength Grating. *Nanomaterials* **2021**, *11*, 1034. [CrossRef] [PubMed]
8. Zhang, X.; Yang, S.; Yue, W.; Xu, Q.; Tian, C.; Zhang, X.; Plum, E.; Zhang, S.; Han, J.; Zhang, W. Direct Polarization Measurement Using a Multiplexed Pancharatnam–Berry Metahologram. *Optica* **2019**, *6*, 1190. [CrossRef]
9. Ji, R.; Xie, X.; Guo, X.; Zhao, Y.; Jin, C.; Song, K.; Wang, S.; Yin, J.; Liu, Y.; Jiang, C.; et al. Chirality-Assisted Aharonov–Anandan Geometric-Phase Metasurfaces for Spin-Decoupled Phase Modulation. *ACS Photonics* **2021**, *8*, 1847–1855. [CrossRef]
10. Ji, R.; Song, K.; Guo, X.; Xie, X.; Zhao, Y.; Jin, C.; Wang, S.; Jiang, C.; Yin, J.; Liu, Y.; et al. Spin-Decoupled Metasurface for Broadband and Pixel-Saving Polarization Rotation and Wavefront Control. *Opt. Express* **2021**, *29*, 25720–25730. [CrossRef]
11. Wen, D.; Pan, K.; Meng, J.; Wu, X.; Guo, X.; Li, P.; Liu, S.; Li, D.; Wei, B.; Xie, X.; et al. Broadband Multichannel Cylindrical Vector Beam Generation by a Single Metasurface. *Laser Photonics Rev.* **2022**, *16*, 2200206. [CrossRef]
12. Ming, Y.; Intaravanne, Y.; Ahmed, H.; Kenney, M.; Lu, Y.; Chen, X. Creating Composite Vortex Beams with a Single Geometric Metasurface. *Adv. Mater.* **2022**, *34*, 2109714. [CrossRef] [PubMed]
13. Han, J.; Intaravanne, Y.; Ma, A.; Wang, R.; Li, S.; Li, Z.; Chen, S.; Li, J.; Chen, X. Optical Metasurfaces for Generation and Superposition of Optical Ring Vortex Beams. *Laser Photonics Rev.* **2020**, *14*, 2000146. [CrossRef]
14. Li, Z.; Liu, W.; Cheng, H.; Choi, D.; Chen, S.; Tian, J. Spin-Selective Full-Dimensional Manipulation of Optical Waves with Chiral Mirror. *Adv. Mater.* **2020**, *32*, 1907983. [CrossRef] [PubMed]
15. Intaravanne, Y.; Han, J.; Wang, R.; Ma, A.; Li, S.; Chen, S.; Chen, X. Phase Manipulation-Based Polarization Profile Realization and Hybrid Holograms Using Geometric Metasurface. *Adv. Photonics Res.* **2021**, *2*, 2000046. [CrossRef]
16. Zhou, H.; Li, X.; Xu, Z.; Li, X.; Geng, G.; Li, J.; Wang, Y.; Huang, L. Correlated Triple Hybrid Amplitude and Phase Holographic Encryption Based on a Metasurface. *Photon. Res.* **2022**, *10*, 678–686. [CrossRef]
17. Georgi, P.; Wei, Q.; Sain, B.; Schlickriede, C.; Wang, Y.; Huang, L.; Zentgraf, T. Optical Secret Sharing with Cascaded Metasurface Holography. *Sci. Adv.* **2021**, *7*, eabf9718. [CrossRef]
18. Song, K.; Su, Z.; Silva, S.; Fowler, C.; Ding, C.; Ji, R.; Liu, Y.; Zhao, X.; Zhou, J. Broadband and High-Efficiency Transmissive-Type Nondispersive Polarization Conversion Meta-Device. *Opt. Mater. Express* **2018**, *8*, 2430–2438. [CrossRef]
19. Dai, Q.; Zhou, N.; Deng, L.; Deng, J.; Li, Z.; Zheng, G. Dual-Channel Binary Gray-Image Display Enabled with Malus-Assisted Metasurfaces. *Phys. Rev. Appl.* **2020**, *14*, 034002. [CrossRef]
20. Chen, K.; Xu, C.; Zhou, Z.; Li, Z.; Chen, P.; Zheng, G.; Hu, W.; Lu, Y. Multifunctional Liquid Crystal Device for Grayscale Pattern Display and Holography with Tunable Spectral-Response. *Laser Photonics Rev.* **2022**, *16*, 2100591. [CrossRef]
21. Deng, J.; Yang, Y.; Tao, J.; Deng, L.; Liu, D.; Guan, Z.; Li, G.; Li, Z.; Yu, S.; Zheng, G.; et al. Spatial Frequency Multiplexed Meta-Holography and Meta-Nanoprinting. *ACS Nano* **2019**, *13*, 9237–9246. [CrossRef] [PubMed]
22. Li, Z.; Chen, C.; Guan, Z.; Tao, J.; Chang, S.; Dai, Q.; Xiao, Y.; Cui, Y.; Wang, Y.; Yu, S.; et al. Three-Channel Metasurfaces for Simultaneous Meta-Holography and Meta-Nanoprinting: A Single-Cell Design Approach. *Laser Photonics Rev.* **2020**, *14*, 2000032. [CrossRef]
23. Wen, D.; Cadusch, J.J.; Meng, J.; Crozier, K.B. Vectorial Holograms with Spatially Continuous Polarization Distributions. *Nano Lett.* **2021**, *21*, 1735–1741. [CrossRef] [PubMed]

24. Zhao, R.; Sain, B.; Wei, Q.; Tang, C.; Li, X.; Weiss, T.; Huang, L.; Wang, Y.; Zentgraf, T. Multichannel Vectorial Holographic Display and Encryption. *Light Sci. Appl.* **2018**, *7*, 95. [CrossRef]
25. Balthasar Mueller, J.P.; Rubin, N.A.; Devlin, R.C.; Groever, B.; Capasso, F. Metasurface Polarization Optics: Independent Phase Control of Arbitrary Orthogonal States of Polarization. *Phys. Rev. Lett.* **2017**, *118*, 113901. [CrossRef] [PubMed]
26. Cai, J.; Zhang, F.; Pu, M.; Chen, Y.; Guo, Y.; Xie, T.; Feng, X.; Ma, X.; Li, X.; Yu, H.; et al. All-Metallic High-Efficiency Generalized Pancharatnam–Berry Phase Metasurface with Chiral Meta-Atoms. *Nanophotonics* **2022**, *11*, 1961–1968. [CrossRef]
27. Zheng, G.; Mühlenbernd, H.; Kenney, M.; Li, G.; Zentgraf, T.; Zhang, S. Metasurface Holograms Reaching 80% Efficiency. *Nat. Nanotech* **2015**, *10*, 308–312. [CrossRef] [PubMed]
28. Bai, G.D.; Ma, Q.; Li, R.Q.; Mu, J.; Jing, H.B.; Zhang, L.; Cui, T.J. Spin-Symmetry Breaking Through Metasurface Geometric Phases. *Phys. Rev. Appl.* **2019**, *12*, 044042. [CrossRef]
29. Bliokh, K.Y.; Gorodetski, Y.; Kleiner, V.; Hasman, E. Coriolis Effect in Optics: Unified Geometric Phase and Spin-Hall Effect. *Phys. Rev. Lett.* **2008**, *101*, 030404. [CrossRef]
30. Deng, Z.-L.; Wang, Z.-Q.; Li, F.-J.; Hu, M.-X.; Li, X. Multi-Freedom Metasurface Empowered Vectorial Holography. *Nanophotonics* **2022**, *11*, 1725–1739. [CrossRef]
31. Wan, W.; Yang, W.; Feng, H.; Liu, Y.; Gong, Q.; Xiao, S.; Li, Y. Multiplexing Vectorial Holographic Images with Arbitrary Metaholograms. *Adv. Opt. Mater.* **2021**, *9*, 2100626. [CrossRef]
32. Zhou, J.; Zhao, J.; Wu, Q.; Chen, C.; Lei, M.; Chen, G.; Tian, F.; Liu, Z. Nonlinear Computational Edge Detection Metalens. *Adv. Funct. Mater.* **2022**, *32*, 2204734. [CrossRef]
33. Kanwal, S.; Wen, J.; Yu, B.; Chen, X.; Kumar, D.; Kang, Y.; Bai, C.; Ubaid, S.; Zhang, D. Polarization Insensitive, Broadband, Near Diffraction-Limited Metalens in Ultraviolet Region. *Nanomaterials* **2020**, *10*, 1439. [CrossRef] [PubMed]
34. Tsilipakos, O.; Kafesaki, M.; Economou, E.N.; Soukoulis, C.M.; Koschny, T. Squeezing a Prism into a Surface: Emulating Bulk Optics with Achromatic Metasurfaces. *Adv. Opt. Mater.* **2020**, *8*, 2000942. [CrossRef]
35. Palik, E.D. Handbook of optical-constants. *J. Optical Society Am. A-Optics Image Sci. Vision* **1984**, *1*, 1297.
36. Prucha, E.J.; Palik, E.D. *Handbook of Optical Constants of Solids*; Academic Press: Cambridge, MA, USA, 1998; Volume 1, pp. 400–406.